Focal control of thalamocortical gain shapes perception

Veronica C. Galvin[1], Anita A. Disney[1]

[1]Department of Neurobiology, Duke University, Durham, NC, 27710
Corresponding author email address: anita.disney@duke.edu

Acknowledgements: This work was supported by NIH grants R01EY029663 to AAD and F32EY034772 to VCG. The authors gratefully acknowledge the assistance of L. Beaver, J. Amodeo, T. Nguyen, K. Coates and A. Brigande and the veterinary and husbandry staff of the Duke Primate Vivarium.
Author Contributions: AAD designed the experiments, developed the adaptation of the normalization model, and assisted with analysis. VCG executed the experiments and analyzed the data. AAD and VCG co-wrote the manuscript.

Abstract
The convergence of sensory and modulatory inputs in cortical layer 4 establishes a point of control with powerful potential: what passes through this gate determines, for all downstream circuits, what exists in the world. Altering the processing state at even a small number of layer 4 synapses should thus be profoundly impactful. We tested this prediction by delivering nicotine in layer 4C of macaque primary visual cortex (V1) while recording across the full cortical depth. The resulting gain pulse, confined to a tiny tissue volume, produced widespread, heterogeneous gain changes throughout all layers of cortex—effects that were quantitatively predicted by a normalization model with a jointly tuned spatial and orientation gain field. The circuit did not compensate for these changes, and so they propagated to bias perceived contrast in an orientation-dependent manner, consistent with model predictions. Focal modulation, applied at the cortical gate, thus reshapes both population coding and perception.

Introduction

The convergence, in layer 4 of cortex, of pathways carrying sensory data from the periphery with modulatory systems carrying state information[1–10] yields a powerful architecture for control. Quite literally: What propagates through layer 4—and in what form—determines, from the 'point of view' of the rest of the cortex, what exists in the external world. Under the implied control this convergent anatomy suggests, it is difficult to know to what extent deficits observed under abnormal modulatory conditions arise from failed cognitive processing (as is often assumed[11–14]), versus perfectly good cognition attempting to operate on flawed data. Seizing control of information flow through even a small proportion of layer 4 synapses should thus profoundly impact downstream processing. Importantly, our assertion is not that adding or mimicking sensory data at this point in the circuit is impactful—this seems obviously true; we can perceive small and/or faint stimuli. Accordingly, causal methods that alter spiking irrespective of sensory data—such as electrical and optogenetic stimulation—can reorganize circuit activity, and alter perception and behavior[15–23]. Instead, the claim here is that neuromodulators can modify perception by *altering the processing state*, rather than the processed information.

Testing this hypothesis requires that four conditions be met: We need 1) a circuit in which a modulatory receptor is uniquely expressed at the thalamocortical synapse (and nowhere else nearby), 2) a selective ligand for that receptor, 3) a means to parametrically vary the strength of sensory drive, and 4) a means to read out gain at the neural and behavioral level. In macaque primary visual cortex (V1), β2 subunit-containing (high affinity) nicotinic acetylcholine receptors (nAChRs) are expressed presynaptically on most thalamocortical synapses onto excitatory neurons in the primary thalamic recipient sublayer, 4C; they are sparsely expressed elsewhere in V1[24]. Activating these receptors does not alter activity in layer 4C in the absence of a visual stimulus, but yields a profound, multiplicative increase in visual responses[24]. This mechanism—selectively strengthening ascending drive without increasing overall excitability—provides a unique tool for injecting a gain perturbation at the cortical 'gate'.

One would expect that a modulatory system with receptors expressed at the gate to cortex—as is the case for the cholinergic system—should have the capacity to profoundly impact processing. Indeed, lesions of the basal forebrain (whose afferents deliver all acetylcholine to cortex in non-rodent species) eliminate visual responses for most V1 neurons[25]. However, local delivery of nicotine in macaque V1, <u>without targeting layer 4C</u>, has little to no effect on visual response gain[24] or performance on a visuospatial attention task[26].

Two key questions remain. First: In what form do highly localized gain changes in layer 4C[24] propagate through the V1 circuit? Second: Do these changes measurably alter perception? The answer to the first question is not obvious *a priori*. A naïve feedforward model predicts that enhancement in layer 4C will yield enhancement in downstream layers. This is not a straw man: a 'volume knob' implementation—applying a uniform multiplier across a circuit—is a prominent approach in modeling neuromodulation[27–30].

Normalization models[31,32] predict a more complex outcome. In macaque V1, delivering a small volume of nicotine to layer 4C will yield a gain field with a particular retinotopic position and receptive field tuning. In this case, normalization models[31,32] predict a mixture of enhancement, suppression, and null effects across the population, determined by a neuron's position (in cortex) and its receptive field tuning relative to a) the visual stimulus and b) the neurons to which the gain field was applied.

Recent optogenetic studies show that normalization computations persist when V1 activity is elevated[15] and that this perturbation reshapes population responses[16]. Critically, however, optogenetic stimulation activates neurons directly, without regard to visual information. This is not a test of normalization models of attention, which predict what happens when information *processing*, rather than information itself, is modified.

We delivered small (nL) volumes of nicotine locally to layer 4C to selectively activate thalamocortical nAChRs, while recording neural activity across the full depth of a V1 column. We found that: 1) only visually-driven activity in layer 4C was changed; 2) the induced processing state change yielded widespread, heterogeneous response changes across all layers; and 3) these changes were well captured by a normalization model with a gain field applied focally to the receptive field position and orientation tuning of neurons at the drug delivery site (in layer 4C). Finally, 4) the gain modulation by nicotine altered perceptual performance.

Results

Nicotinic acetylcholine receptors (nAChRs) are expressed at thalamocortical synapses across systems, and their activation strongly enhances gain[5,24,33–36]. However, gain modulation by nicotine has not yet been demonstrated in a behaving animal. We thus first assayed the local (within-layer) effect of activating nAChRs in layer 4C of V1 in awake and fixating rhesus monkeys, using neural contrast responses as a measure of gain (Fig. 1).

We used 32-channel electrode arrays (Plexon, S-probe) equipped with a fluid capillary (Fig. 1C) to deliver nicotine and simultaneously record from the entire cortical depth of V1 across 9 sessions (4 from Monkey D, male; 5 from Monkey E, female). We positioned the fluid capillary exit ('fluid port') in layer 4C based on current source density analysis of visually-evoked local field potentials (Fig. 1C).

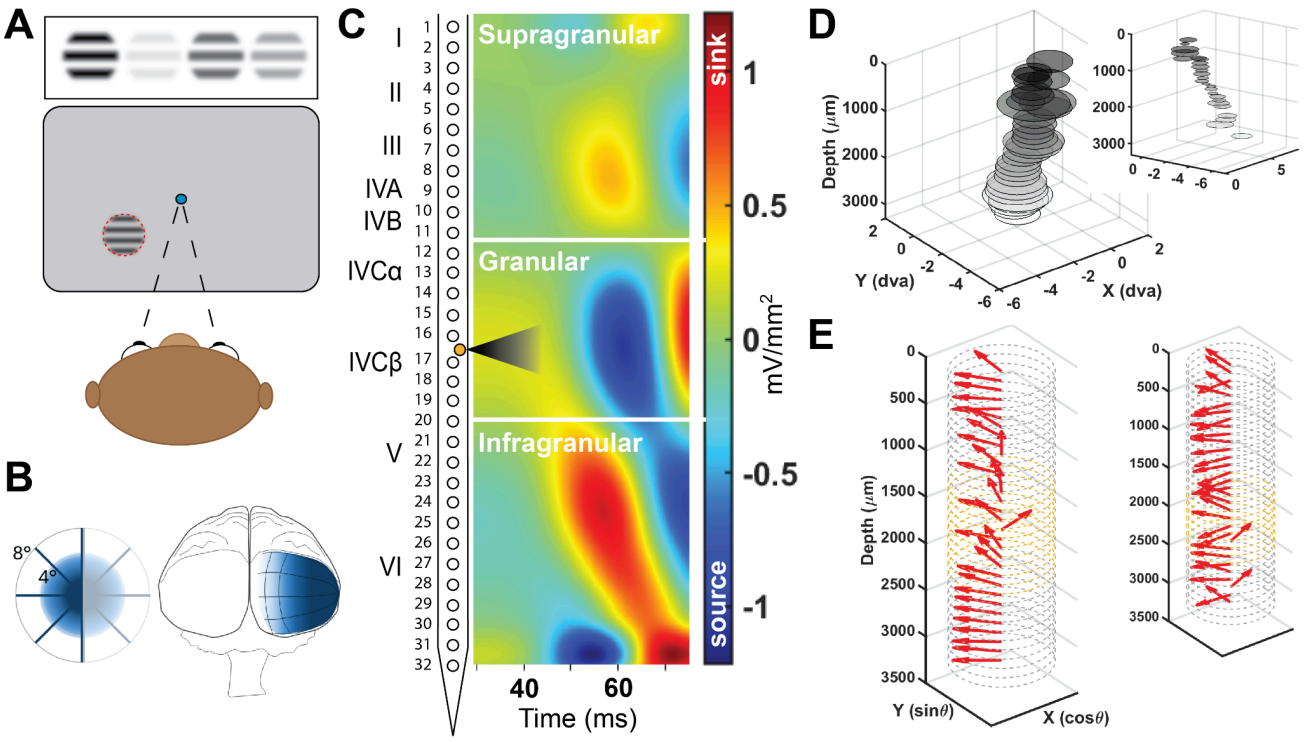

Figure 1. Experimental Design. (A) Task schematic: Monkeys fixate centrally (blue dot; accuracy window 1° visual angle, dva) while Gabor stimuli are used to measure receptive field position (red dashed circle), orientation tuning, and contrast responses. **(B)** Recording sites were in parafoveal (<8° eccentricity) V1. **(C)** Electrode arrays were inserted perpendicular to the brain surface and spanned the full cortical depth (left). A fluid capillary exit on the array (orange circle) was positioned in layer 4C by current source density analysis of visually-evoked local field potentials and nicotine delivered by pressure ejection (black triangle). **(D)** Receptive field alignment for our most (main) and least (inset) aligned (with the cortical column) recording days. Depth axis: 0 = ~pia; 3200 μm = channel 32. Position: dva from fixation. **(E)** Preferred orientation (red arrows; circles: 360° of direction tuning) at each channel for the days shown in D is consistent with columnar recording. Yellow dashed circles: layer 4C.

The local effect of nicotine in layer 4C

After excluding recording sites that were visually unresponsive, poorly tuned, and/or unstable under pressure ejection (see Methods), we had 160 recordings (Monkey D: 75; Monkey E: 85) available for our main analysis of nicotine effects, and a further 28 recordings from a stationarity control study (Monkey E). Of the 160 recordings (mostly multi-unit, MU) in the main analysis, 77 were in the supragranular layers (2-4B), 39 in the granular layer (4C), and 44 in the infragranular layers (5, 6).

We saw a striking increase in layer 4C spiking activity when we delivered nicotine (Figure 2A,B; yellow asterisks), similar in magnitude and form to the gain enhancement observed in layer 4C of macaque V1 under

anesthesia[24]. Attributing these changes to nicotine itself requires demonstrating 1) recording stationarity and 2) a lack of gain changes during delivery of the diluent (saline).

Recordings are stationary during saline delivery

Delivering fluids by pressure ejection can cause a loss of unit isolation hundreds of microns away[37,38]. Each recording day, we started by measuring neural contrast responses over a series of saline controls with increasing ejection pressure. We lost all but 3 well-isolated units during these controls. Note that assessing pharmacological manipulations using MU activity is conservative; drug effects must be substantial to appear in collective measures of neural activity.

We carefully optimized delivery parameters (see Methods), resulting in excellent stationarity after the first few saline 'pulses' (Fig. 2B-D; note range of S:S values in 2B). For each day, we capped the backing pressure for nicotine at the highest pressure yielding stable recordings with saline, and set spike sorting parameters from this stable saline condition, which serves as the control in all analyses below. On a dedicated, saline-only 'stationarity control' day, stability lasted the full ~2-hour recording (28 units; Fig. 2C, Supp. Fig. S1).

Nicotine selectively alters visual responses

As expected for gain control by neuromodulation, 'spontaneous' activity in layer 4C (mean response to blank screen trials interleaved amongst the sequence of Gabor stimuli) was unchanged by nicotine: saline average spikes/sec = 6.93 (sd = 9.06); nicotine = 7.21 (sd = 9.64; paired t-test: $t(38) = -0.267$, $p = 0.7908$).

A contrast response function (CRF; Fig. 2B, insets) quantifies the relationship between stimulus intensity and spiking response. As a non-parametric measure of gain, we calculated a 'ratio of normalized response areas' (RA) under the CRF: for each contrast, under two conditions to be compared, we calculated the average firing rate, subtracted the blank-screen response, normalized to the 96% contrast response in the saline condition, summed across contrasts, and expressed the result as a ratio (e.g., nicotine/saline; N:S or first/last saline block S:S)[24].

On the background described above—weak, stable 'suppression' (loss of unit isolation) with saline delivery—the ratio of the pressure-matched nicotine and saline conditions (N:S RA) in layer 4C <u>increased</u> across the population (average N:S RA = 1.610; SEM ± 0.33; yellow asterisks, Fig. 2A,B). Unlike responses to saline delivery, responses to nicotine were often non-stationary; the resulting high variance over trials precluded significance testing on individual units. We thus used the range of effect magnitudes observed in the stationarity control study (S:S RA, 0.64 to 1.46; dotted vertical lines, Fig. 2A) to classify units as individually 'enhanced' or 'suppressed'. For the 12 enhanced layer 4C units (N:S RA > 1.46), the median RA was 2.52 (mean = 3.682). A further 10 units were suppressed (N:S RA < 0.64; median RA = 0.421, mean = 0.371). The remaining 17 were classified as showing no effect of nicotine delivery.

We tested up to three nicotine 'doses' (backing pressure levels); the population N:S RA in layer 4C increased with dose (Fig. 2A, middle inset). Nicotine is lipophilic and persists after ejection; N:S RA did not return to baseline over the 7-15 minutes of recovery possible within a recording day (recovery to saline, R:S RA, t-test vs. 1: $t(38) = -2.619$, $p = 0.0126$). Consistent with a ligand-specific effect, the lack of recovery was restricted to enhanced units (R:S RA vs. 1: $t(11) = 3.412$, $p = 0.0058$); the 10 suppressed units <u>did</u> recover (R:S RA vs. 1: $t(9) = -1.422$, $p = 0.1887$), consistent with suppression being a network effect (see below) rather than continued loss of unit isolation.

Delivering nicotine to layer 4C has heterogeneous effects in other layers

The magnitude and direction of the RA change in layer 4C with nicotine delivery were similar to our prior study[24], so we asked what happens in the supragranular (2-4B) and infragranular (5,6) layers that receive this modified activity as feedforward drive. As in layer 4C, nicotine did not change spontaneous activity for supragranular units (saline = 9.74 spikes/sec, sd = 10.64; nicotine = 10.82, sd = 12.66; $t(76) = -1.062$, $p = 0.2916$). However, nicotine <u>did</u> increase spontaneous activity in the infragranular layers (saline = 6.42 spikes/sec, sd = 6.36; nicotine = 9.54, sd = 9.62; $t(43) = -3.103$, $p = 0.0034$; see Discussion). Spontaneous activity in the infragranular layers did not recover ($t(43) = -2.60$, $p = 0.0127$), and was confined to enhanced units, i.e., those for which blank-subtracted activity was also increased.

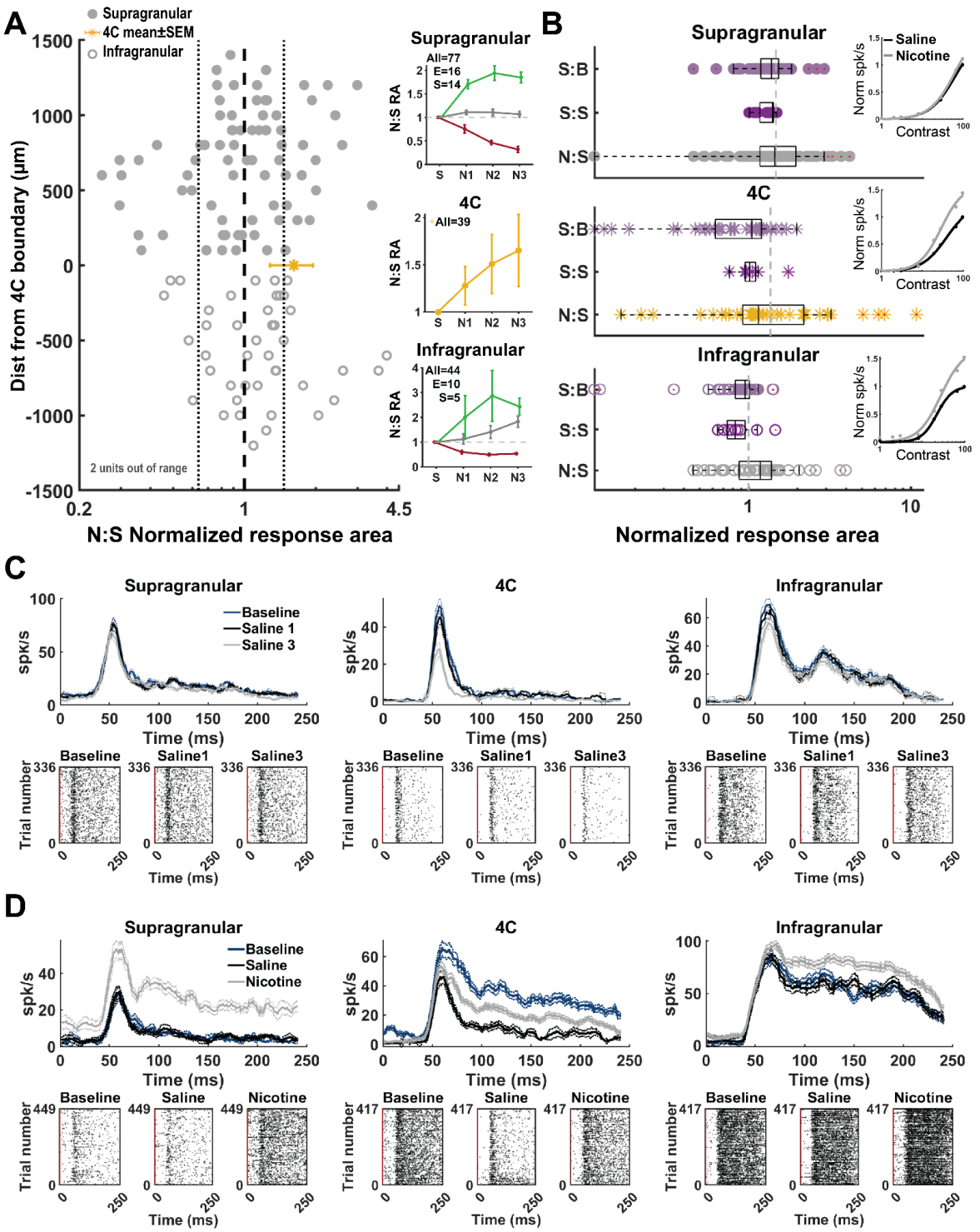

Figure 2. Nicotine enhances gain in layer 4C, and the effect propagates. (A) Nicotine to saline (N:S) response area (RA) as a function of distance from the layer 4C boundary. Yellow asterisk: layer 4C mean ± SEM (n=39). Filled circles: supragranular (n=77); open circles : infragranular (n=44). Dashed line: RA = 1, i.e., no difference in normalized, blank-subtracted, total spike count between the conditions. Dotted lines: S:S RA range from stationarity control (Supplementary Fig. S1). n=121 units, 2 animals. Insets: 'Dose' response curves, see text. Yellow: all units, layer 4C. Gray: all units, extragranular layers. Green (E): RA>1.46. Red (S): RA<0.64. **(B)** RA ratio by laminar category and condition. Boxplots: median and IQR. Light purple: saline to (no fluid ejection) baseline, S:B; dark purple: first to last saline block, S:S; yellow (4C) and gray (extragranular): N:S. RA variance differed across conditions (Bartlett's test, all $p < 10^{-12}$). Insets: population contrast response function fits (gray: nicotine; black: saline). **(C)** Example recordings showing stationarity under repeated saline delivery. Top: spike density functions (sliding window average, ± SEM) for no fluid delivery baseline (dark blue), first saline (black), and last saline (light gray) block. Bottom: Raster plots aligned to stimulus onset (t=0; red line). **(D)** Example recordings showing nicotine effects. Conventions as in C; light gray is the pressure-matched nicotine condition.

The effect of delivering nicotine to layer 4C on visually driven activity in other layers varied enormously (N:S RA range: 0.13-3.98). Again using the S:S RA range to classify units, we identified 16 enhanced (median N:S RA = 1.99) and 14 suppressed (median = 0.362) supragranular units, with 47 showing 'no net effect' (see below). In the infragranular layers, we identified 10 enhanced (median N:S RA = 2.08), 5 suppressed (median = 0.534), and 29 no net effect units. Gain changes were uncorrelated with distance from the drug delivery site (supragranular Spearman's $\rho = 0.115$, $p = 0.371$; infragranular $\rho = 0.013$, $p = 0.935$; Fig. 2A). The 'no net effect' classification outside layer 4C is distinct from 'no effect' in 4C: extragranular neurons are not directly affected by nicotine, so an unchanged N:S RA reflects precisely balanced enhancement and suppression (see normalization model below); no *net* effect.
Dose response curves within gain change classes were roughly monotonic (Fig. 2A, insets), with some 'saturation' (changing enhancement/suppression balance). Unit-by-unit analysis revealed 5 enhanced units (3 supragranular, 2 infragranular) with inverted U-shaped dose responses. In the analyses below, we use the same pressure-matched nicotine condition for all units; for these 5 units this is not the peak gain response.

Receptive field position and tuning do not explain gain heterogeneity

We wondered whether the pattern across the population of enhancement versus suppression might be explained by individual units being strongly or poorly driven by the chosen 'best match' stimulus (see Methods). Neither change magnitude nor direction was correlated with the difference between a unit's preferred orientation and the stimulus orientation (Fig. 3A), nor with receptive field (RF) overlap (Fig. 3B). Note that units with 100% RF overlap showed the the full range of N:S RA magnitudes (Fig. 3B, inset). This result is not changed if we restrict the analysis to 'well-driven' units (see Supplementary Fig. S2).

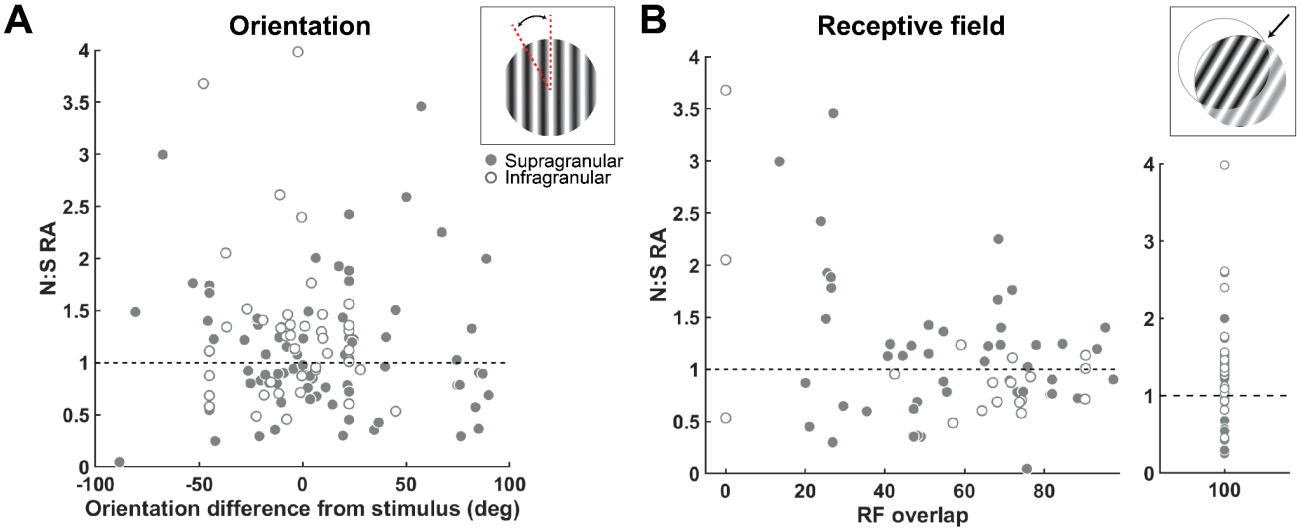

Figure 3. Gain change magnitude is unrelated to receptive field (RF) tuning. **(A)** Response area (N:S RA) vs. orientation difference from stimulus (degrees). Filled: supragranular (n=77); open: infragranular (n=44). Dashed: RA = 1. **(B)** Response area vs. RF overlap. Inset: units with 100% overlap.

Mixed gain effect types

A parametric analysis of the relationship between stimulus contrast and firing rate can be achieved by fitting a model function to the data (insets, Fig. 2B)[24,39,40]. We fit neural CRFs to a hyperbolic ratio function (see Methods) that yields four parameters: slope (n), asymptotic firing rate (Rmax), contrast at half maximum firing rate (c50), and offset (sFR). Changes in the Rmax and c50 parameters are often used to assess 'response' (Rmax) versus 'contrast' (c50) gain. We analyzed bootstrapped fits (1000 resamples) to individual neurons' CRFs (77 supragranular and 44 infragranular) and tested for significant parameter changes using Wilcoxon rank-sum tests. After FDR correction, 110/121 units (91%) showed significant Rmax changes (Fig. 4A, left); of

119 units for which c50 was well-constrained, 80 (67%) showed significant c50 changes (Fig. 4A, right). Across the population, we observed four gain change types: response gain only (31%), contrast gain only (6%), mixed (60%), and no change (3%). Despite the high prevalence of individually significant changes, the population-level shift in Rmax was modest (saline median = 40.3; nicotine = 45.4 spikes/sec; Fig. 4B, left), and the population c50 was unchanged (saline = 27.4%; nicotine = 27.6% contrast; Fig. 4B, right). The normalization model of attention we apply below provides a framework for understanding this pattern.

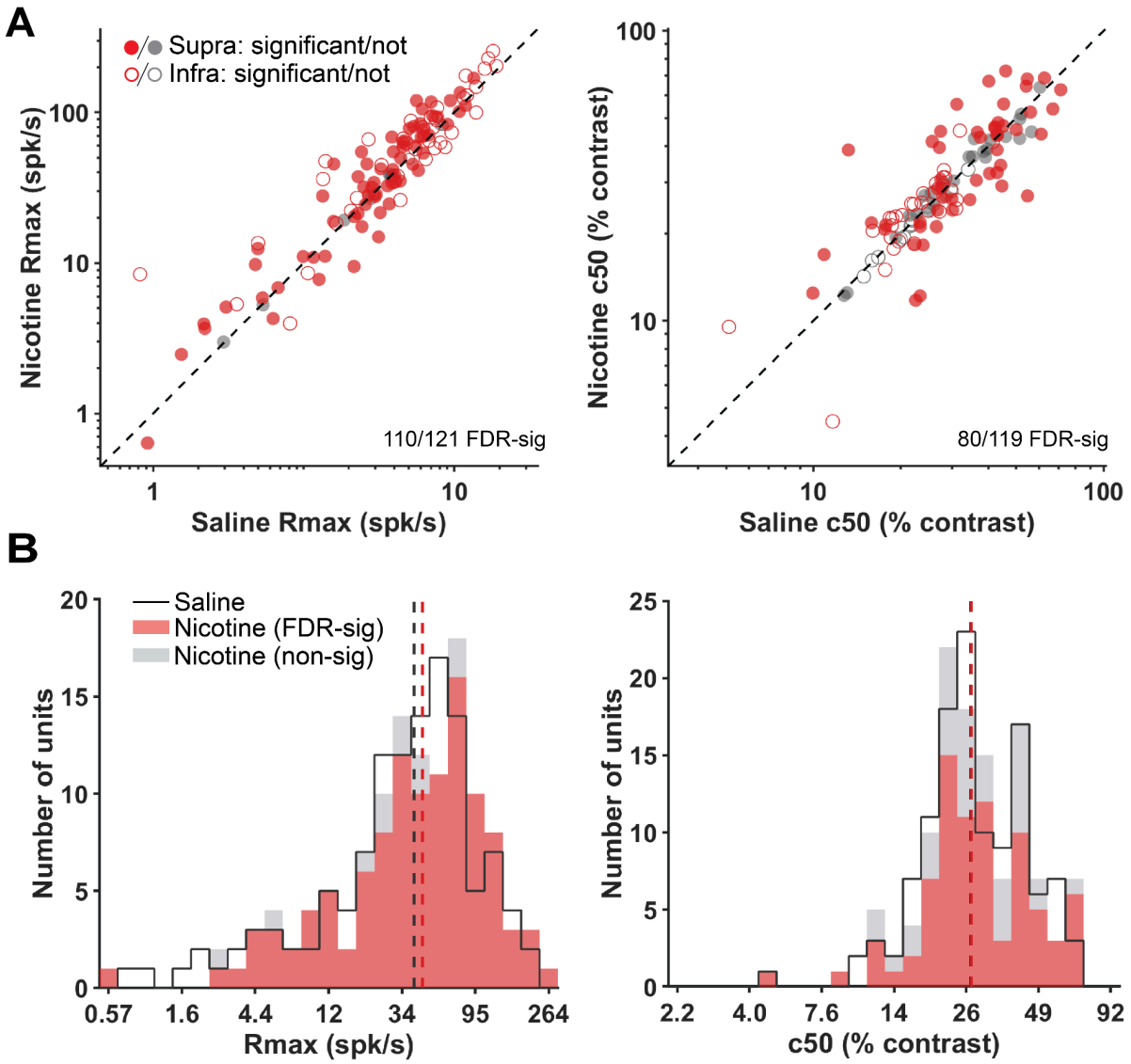

Figure 4. Parametric gain change analysis. (A) Median fit values for Rmax (left) and c50 (right) in the nicotine (y-axis) vs saline (x-axis) conditions for supragranular (filled circles, n=77) and infragranular (open circles, n=44) units. Red: units with significant median differences (rank-sum test with FDR correction); gray: non-significant differences. Dashed line: unity. **(B)** Histograms of median fit values for Rmax (left) and c50 (right) in the saline (black, unfilled) condition, and for units with significant (red) and non-significant (gray) differences, collapsed over laminar categories. Black (saline) and red (nicotine) vertical dashed lines: population medians; Rmax: saline = 40.3, nicotine = 45.4; c50: saline = 27.4, nicotine = 27.6.

Applying a normalization model of attention

Thus far, we have attempted to explain our data based on the V1 circuit (e.g., laminar position) or stimulus properties, but these were constants in our experiment—what differed was the presence or absence of the focal gain pulse. Normalization models of attention address such a case[31,41], predicting a multiplicative response gain change—as observed here for layer 4C—in the regime where stimulus >> attention field size.

That is, when the number of neurons responding to the stimulus is larger than the number of neurons subject to the gain field. We wondered whether this framework could account for the pattern of effects across our population.

We applied Reynolds and Heeger's implementation of a normalization model of attention[31], using the authors' publicly available code (see Methods). In their model, the response, R, of a neuron with RF visual position x and preferred orientation θ is:

$$R(x\theta) = |[A(x,\theta)E(x,\theta)]/[S(x,\theta) + \sigma]|_T \qquad \text{Eq. 1}$$

This roughly states that the response R(x,θ) is proportional to excitatory drive E(x,θ) scaled by an attention (here, nicotine) gain field A(x,θ), and divisively normalized by a pooled suppressive drive S(x,θ) plus a semisaturation constant σ. In this formulation, the normalization pool sees the product of attention and stimulus, not each independently. The multiplicative relationship between the gain field and excitatory drive is difficult to test causally: methods like optogenetic stimulation add stimulus-independent activity (effectively $[A(x,\theta) + E(x,\theta)]$). However, in activating receptors *selectively expressed on thalamic axons*, in a manner that yields a response gain increase on the visual response only, we achieve the specified multiplicative ($[A(x,\theta) * E(x,\theta)]$) interaction.

Critical to our model adaptation was accounting for the fact that, unlike traditional attention tasks in which the stimulus field (excitatory drive) and attention field are co-located (as a result of 'attending to' the stimulus), our stimulus and gain fields are misaligned. Further, our recorded neurons vary in position and tuning with respect to both these fields, and the misalignments differ in form across days (Fig. 1D,E; Fig. 5).

To apply the model, we treated nicotine as delivering a gain field, the tuning of which was determined by the layer 4C neurons nearest the fluid port on the electrode array. We mapped this gain field, and each unit's RF location and orientation preference, into the model's coordinate space (x,θ). RF positions were projected onto an axis running from the fixation point through the stimulus center (yielding x in arbitrary units ~2 * eccentricity). Orientation preferences were expressed as deviations from the stimulus (stimulus θ = 0°).

For each recording day, we fit four parameters describing the nicotine gain field (Table 1), optimizing them to predict the classified N:S RA for each unit (ternary labels: enhanced [+1], N:S RA > 1.01; suppressed [-1], N:S RA < 0.99; no net effect [0], N:S RA = 1). A further five 'global' parameters (shared across days) were then fit to the full dataset: gain field size (AxWidth) for saline and nicotine, gain field tuning bandwidth (AθWidth) for saline, and model neuron orientation tuning bandwidth (EθWidth, IθWidth). A final per-day refit followed with global parameters fixed.

Table 1: Per-day parameters.

	Nicotine concentration (mM)	**Gain field peak (Apeak)**	**Gain field position (Ax, Stimx*)**	**Gain field tuning (Aθ; degrees)**	**Gain field bandwidth (AθWidth; degrees)**
April 26	500	5.3	8,8	-5	12
Dec 10	200	7.2	2,4	-16	12
Feb 08	400	1.5	4,4	29	12
Jan 13	400	4.0	4,4	22	4
Jan 20	400	1.3	12,10	-26	4
Jun 11	400	1.4	5,6	-148	12
Jun 20	300	2.2	3,4	13	4
May 16	250	8.0	10,10	-55	12

* RF positions were projected onto an axis running from fixation through the center of the stimulus position (Stimx), see Methods. Arbitrary units (AU), ~2 * eccentricity in degrees of visual angle.

In the final fit, three days had identical, narrow, nicotine gain field tuning bandwidths (AθWidth = 4); three others had broader tuning (AθWidth = 12). The remaining two days also had broad bandwidths (AθWidth = 13 and 17 for Jun 11 and Feb 8, respectively). Simplifying to two values did not importantly alter prediction accuracy (defined below; 1 newly misclassified unit of 121), so the simplified solution was adopted. The global parameter values were: AxWidth, nicotine = 2.4, saline = 7.5; saline AθWidth = 90º; EθWidth = 50º; IθWidth = 70º (see Supplementary Table 1 for all global values, fixed and fit).

The result is a unique model implementation for each recording day (Fig. 5). For a given RF position, the model predicts a mix of enhancement, suppression, and net-zero gain effects, largely determined by a neuron's orientation tuning (Fig. 5B). The absence of structure in Figure 3A may appear to contradict Figure 5B. Note that in Figure 3A data are presented for all 8 days, destroying the structured variation evident in the per-day data.

Across RF positions, the model produces a family of predicted gain curves for the nicotine and saline conditions (curves in Fig. 5B are for x=4, the stimulus position). The difference (nicotine minus saline) between these curves, across RF positions, defines a surface (Fig. 5C). Note that we sample only a subregion of this surface (colored in Fig. 5C). The model-predicted gain effects can then be compared to the data (Fig. 5D,E). On the day presented in Figure 5 (Dec 10), depending on the accuracy measure (firing rate at 96% contrast versus N:S RA), ~88-94% of neurons (i.e., 15/17 or 16/17) were correctly classified. Furthermore, predicted versus observed gain magnitudes were correlated (96% contrast: Spearman's $\rho = 0.481$, $p = 0.0508$, $n = 17$; RA: $\rho = 0.516$, $p = 0.0339$, $n = 17$); recall that only permissive ternary labels (0.99 and 1.01 cutoffs) were fit.

On one recording day (May 16), the fluid port was in layer 4B. For each day, we used the orientation tuning at electrodes 16 and 17 (adjacent to the fluid port) to set priors on gain field orientation tuning, Aθ. However, nAChRs are sparsely expressed in layer 4B of macaque V1[24]; accordingly, model fitting for May 16 converged on a value for Aθ that reflected *tuning at the nearest layer 4C sites* (electrodes 18/19; preferred θ = 103°/106°; Aθ = -55° with respect to the stimulus θ = 157.5°; Table 1), not the tuning of the units around the port (θ = 161°/151°; Aθ ≈ 0).

Over all 8 days, the model accurately predicted ternary effect class for 83% (peak contrast response; Fig. 6A) or 84% (N:S RA; Fig. 6B) of 121 units. Accuracy dropped significantly for shuffled ternary labels (peak contrast: mean = 63.2%, sd = 3.3%, $p = 0.0001$; N:S RA: mean = 62.7%, sd = 3.4%, $p = 0.001$; 10,000 iterations; Supplementary Fig. S3). In our shuffling approach (randomizing ternary labels), the null distribution mean (~63%) reflects chance agreement between predicted and observed marginal class proportions (i.e., the fraction of units for each ternary class, on each day). The observed accuracy of 83-84% exceeds this base-rate expectation; the model captures unit tuning structure in nicotine's effects, not just overall prevalence of enhancement and suppression. As in the example day above (Dec 10; Fig 5), although the model was fit to gain class only, predicted and observed gain magnitudes were positively correlated across the population (peak contrast: Spearman's $\rho = 0.599$, $p < 10^{-12}$; RA: $\rho = 0.566$, $p < 10^{-10}$; $n = 121$). The concentration of the nicotine solution differed across days (Table 1); none of the fit parameters were correlated with concentration (Apeak: $\rho = -0.469$, $p = 0.2464$; AθWidth: $\rho = 0.274$, $p = 0.5107$; Ax: $\rho = 0.431$, $p = 0.2893$; Aθ: $\rho = 0.216$, $p = 0.6107$; see Discussion).

There were 21 prediction errors (of 121 units) for peak (96%) contrast and 19 for RA. Setting a 'within measurement noise' tolerance at $0.8 < \text{ratio} < 1.2$ (~half the S:S RA range, Fig. 2), 9 of 21 peak-response errors and 4 of 19 RA errors fell within this range. Of the remaining errors, 10 were recordings with poorly defined orientation tuning (2 peaks, or a broad 'peak').

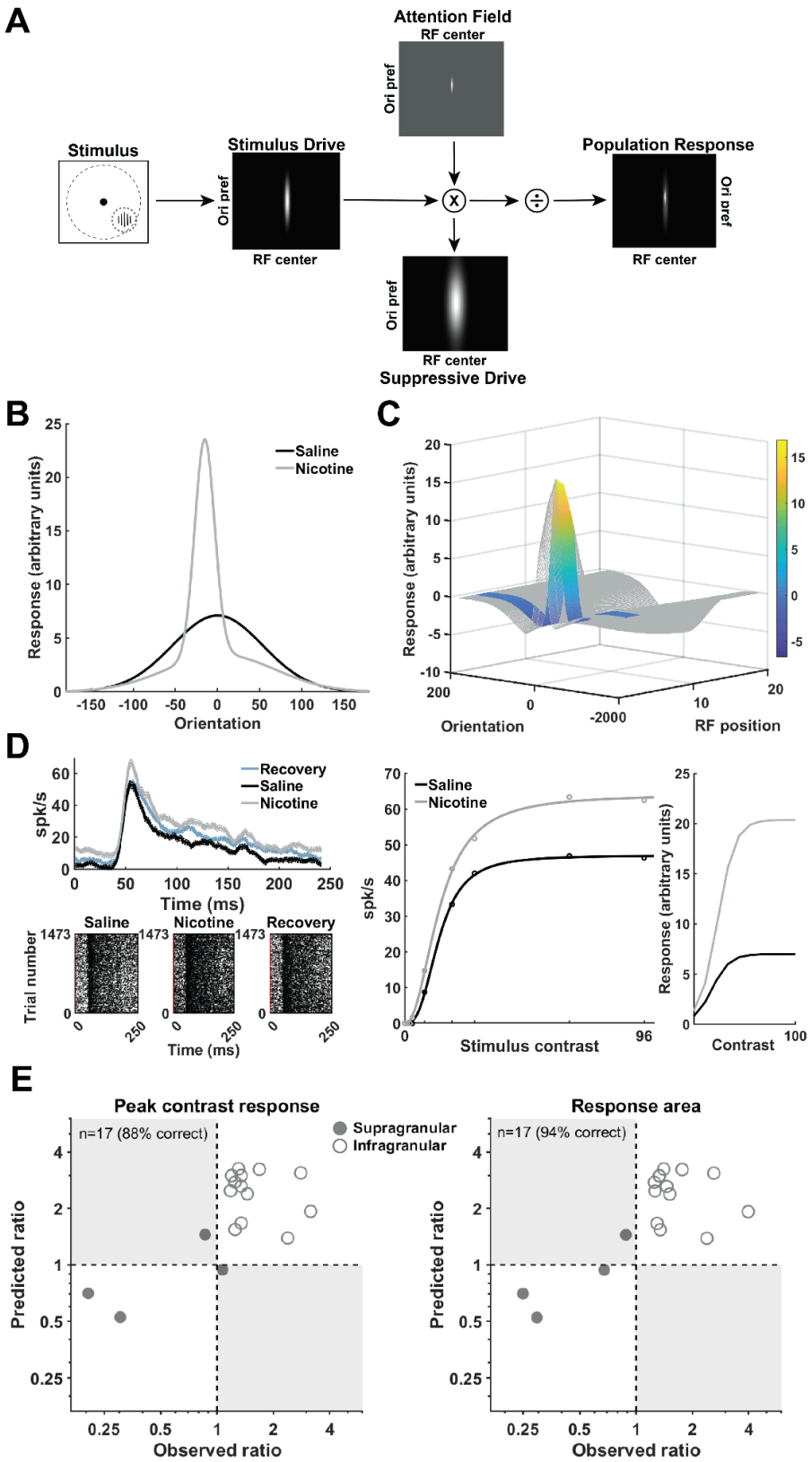

Figure 5. Adapted normalization model, example day (Dec 10; Monkey D). (A) Model schematic adapted from Reynolds and Heeger[31], showing a localized gain field (Attention Field', top) in position (x) and orientation (θ). **(B)** Predicted gain curves at the stimulus position (x=4). **(C)** Full predicted gain change (nicotine minus saline) surface over orientation and receptive field position; colored region: range sampled by our array. **(D)** Example enhanced unit. Left: spike density functions (sliding window average ± SEM; top) and rasters (below). Center: observed contrast responses, with fits. Right: model-predicted contrast response functions. Black: saline; gray: nicotine; blue: recovery. **(E)** Predicted vs. observed ratio (N:S) for the response to 96% contrast (left; 88% correct, 15/17) and RA (right; 94% correct, 16/17). Filled: supragranular; open: infragranular.

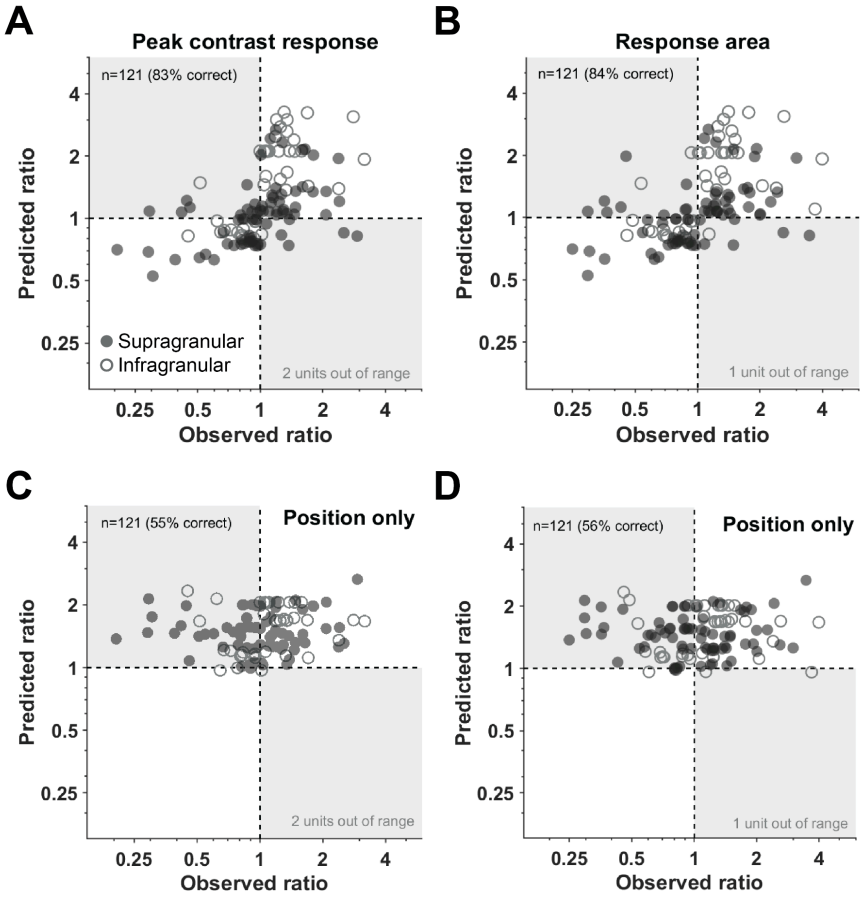

Figure 6. Model predicted versus observed gain changes across the population. (A) Observed (x-axis) versus predicted (y-axis) ratio of the response to 96% contrast. White regions: predicted and observed change classes agree; gray regions: predicted and observed classes differ. Filled circles: supragranular; open circles: infragranular. **(B)** Observed versus predicted ratio for response area (N:S RA), conventions as in A. (**C**) As in A (peak contrast prediction accuracy) for a model with position information only. (**D**) As in B (N:S RA accuracy), model with position information only.

A sensitivity analysis (Supplementary Fig. S4) suggested that model performance was sensitive to gain field orientation tuning. We evaluated a position-only variant of the model in which the gain field was untuned (AθWidth = 180°), with all other parameters unchanged. This model achieved 55.4% accuracy for the peak response (Fig. 6C) and 56.2% for RA (Fig. 6D)—well below the shuffled-label null (63.2%) and full model (82.6-84.3%). Of 48 units for which the variants disagreed, the full, joint (orientation and position) model was correct for 40, the position-only model for 7. Predicted and observed gain magnitudes were uncorrelated for the position-only model (peak contrast: $\rho = 0.163$, $p = 0.075$; RA: $\rho = 0.112$, $p = 0.222$). An inability to properly define a preferred orientation is thus expected to undermine prediction accuracy.

This left six well-tuned units (of 21 mis-predicted units) with substantive prediction errors for both peak contrast and RA. One was clearly lost during recording (final N:S RA 0.05). Another three had very large orientation preference deviations from the stimulus (> 135°), placing them in a low firing rate regime in which single spikes can alter observed ternary class; all three were predicted ‘no effect’ but observed suppressed. Leaving two well-tuned, well-driven mis-predicted supragranular units: For one an enhancement was predicted and no net effect was observed (N:S peak contrast = 0.998; N:S RA = 0.933); for the other no effect was predicted but suppression (N:S peak contrast = 0.427; N:S RA = 0.4591) was observed.

Model-predicted gain types

When stimulus and gain fields are aligned, and the gain field is small, normalization models predict an increase in the fit asymptotic firing rate (Rmax) for the CRF (i.e., response gain). For the misaligned case, these models predict response gain increases and decreases, as a function of orientation (Fig. 5). Of the 110 (of 121) units with significant changes in Rmax (Fig. 4), the predicted and observed gain change direction (increase/decrease) agreed for 90 (81.8%). For c50, on the other hand, the model predicts no change in c50 for any unit, and while the median c50 was unchanged across our population (Fig. 4B, right), we report significant c50 changes for 80 units. For 18 units this may be an artifact of fits yielding an Rmax decrease applied to data with a firing rate floor set by blank-subtraction. For the remaining 62 units, the median population c50 ratio (N:S) was exactly 1.0 (IQR: [0.94, 1.13]). This small IQR relative to saline stationarity (S:S) variability suggests that statistically detectable c50 changes reflect measurement variability rather than a systematic effect. Rmax changes, in contrast, were more substantial and directional (median = 1.1; IQR: [0.94, 1.39]), consistent with the model-predicted predominance of response gain enhancement.

Do infragranular layers 'see' the gain field directly?

The canonical feedforward circuit for macaque V1 describes a projection from layer 4C to the supragranular layers and then to the infragranular layers. However, minor direct projections from layer 4C to the infragranular layers have been described[42–46]. Our model thus far treats all extragranular units identically, essentially assuming direct input from layer 4C to all layers. We tested whether infragranular predictions would improve under a 'cascade' model in which supragranular output mediates the gain signal. Refitting per-day parameters to the 77 supragranular units alone (also allowing EθWidth and IθWidth to vary; remaining global parameters fixed) yielded narrower orientation tuning than fitting to the full population (supragranular-only EθWidth = 20°, IθWidth = 50°) and modestly improved supragranular accuracy (peak contrast/N:S RA: 79%/82%, up from 78%/79%). We then generated out-of-sample predictions for infragranular units, blending direct and cascade models with a mixing parameter α (α = 1: direct model; α = 0: pure cascade). The best infragranular accuracy occurred at α = 0.9, with a prediction accuracy (93.2% N:S RA), identical to the direct model.

The gain effects evident in neural activity impact perceptual performance

Our focal gain injection to layer 4C altered activity across the entire cortical column (Fig. 2). We wondered whether the circuit compensates for these effects, or whether they are evident in behavior. We trained one animal (Monkey E) on a two-alternative forced-choice contrast discrimination task designed to determine the animal's 'point of subjective equivalence' (PSE) between two simultaneously presented static Gabor stimuli of matched size, orientation, and spatial frequency. The task was to saccade to the Gabor with higher apparent contrast (Fig. 7A). We delivered nicotine to layer 4C during task performance over 6 recording days. On three days, the tuning of units near the fluid port (in layer 4C) was within 10º of the onscreen stimuli; on the other three, tuning near the port differed substantially from the stimulus. The normalization model makes predictions for these two session types: when the gain field is co-tuned with the stimulus, nicotine delivery into V1 should *increase* apparent contrast of the stimulus in the contralateral (right) visual hemifield, lowering the PSE and shifting the psychometric curve over contrast leftward (green, Fig. 7B). When the gain field is not co-tuned, nicotine should *reduce* the apparent contrast of a stimulus in the gain field, raising the PSE, and shifting the psychometric curve rightward (red, Fig. 7B). We tested this prediction using a within-session composite measure of the net shift in rightward choice bias under nicotine relative to saline. On all six sessions, the composite score shifted in the direction predicted by the model (sign test, $p = 0.031$; one-sample t-test, $t(5) = 2.44$, $p = 0.059$; Fig. 7C). In the ipsilateral (no drug) visual hemifield, PSE was unchanged (Fig. 7D); in the contralateral (drug affected) hemifield, nicotine shifted the PSE to favor a lower contrast reference stimulus (Fig. 7E).

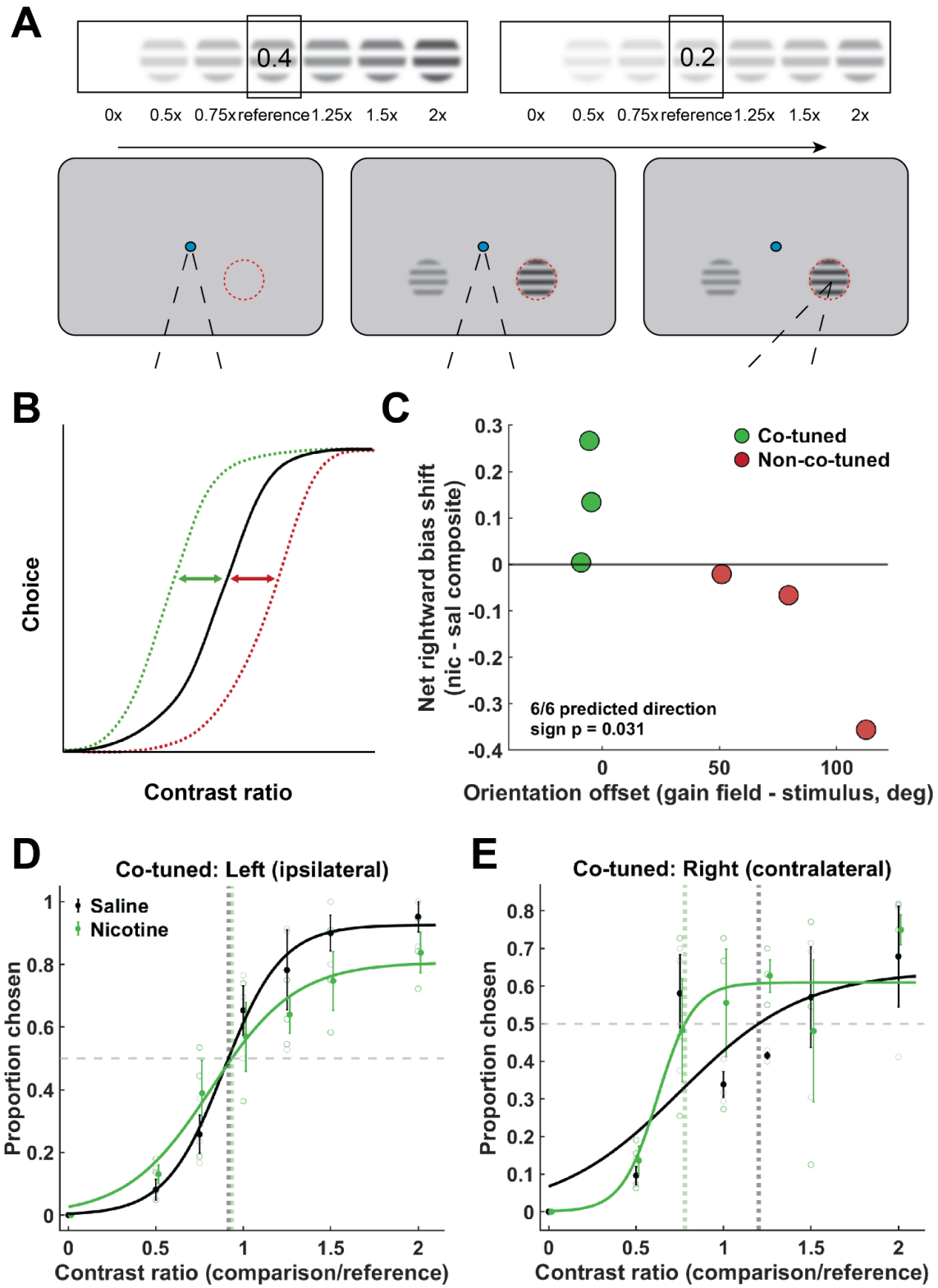

Figure 7. Nicotine alters perceived contrast. (A) Task schematic. Upper: comparison contrasts at half-steps around 20% and 40% references. Lower: trial sequence—fixate, two Gabors appear (one in the gain field, red circle; one at matched eccentricity contralaterally), saccade to higher apparent contrast. **(B)** Predicted psychometric curve shifts: leftward (green) when stimulus and gain fields are co-tuned; rightward (red) when not. **(C)** Net rightward bias shift (nicotine minus saline) vs. orientation offset. All 6 sessions shifted in the predicted direction (sign test, p = 0.031). **(D)** Choice behavior, ipsilateral (control) hemifield, three co-tuned sessions. Filled circles: session mean ± SEM; open circles: individual sessions. Curve: logistic fits to pooled means. Black: saline; green: nicotine. Vertical dashed lines: point of subjective equivalence (PSE). **(E)** Contralateral (drug-affected) hemifield. Nicotine shifted the PSE to lower contrasts. Conventions as in D.

Discussion

We report that delivering a focal gain pulse to cortical layer 4C produces profound, heterogeneous changes in neuronal activity across all layers of V1, changes that are reflected in perceptual performance. The capacity for nicotine to boost local change in layer 4C is conserved across species and sensory systems[5,24,33,34,36]. The *near-exclusive* localization of high-affinity nicotinic receptors (nAChRs) at thalamocortical synapses, in layer 4C of macaque V1 specifically, provides a basis for isolating and interpreting effects in other layers.

Our interpretation focuses on high-affinity nAChRs because expression data for low-affinity (homomeric, α7 subunit) nAChRs is not available for macaque V1 (antibodies have not passed controls in our hands) and because the pattern of nicotine's local effects in other layers mirrors the expression pattern of the high affinity receptors[24]. However, radioligand binding indicates that low-affinity nAChRs are also selectively expressed in layer 4C[4]; they may well contribute to the gain effects we observed. Nicotine induced gain changes hundreds of micrometers away, in supra- and infragranular layers. These distal effects are unlikely to be due to direct nAChR activation outside layer 4C: local nicotine delivery in layers 2–4B, 5, and 6, where nAChR expression is sparse[4,24], does not alter visual responses[24].

The heterogeneous effects we observed following nicotine delivery evidence a complex interplay between inherited gain and local circuitry, and suggest that the endogenous ligand (ACh) probably supports a sophisticated, circuit-dependent computation, not a 'volume control knob'. We showed that this computation involves a gain field that can be modeled by normalization models of attention[31,41], providing, to our knowledge, the first application of these models to circuit level gain field manipulations tuned in both retinotopic and feature space.

A long history of work has examined the dependence of normalization on the stimulus–receptive field relationship[50,51]. Building on this, optogenetics in macaque V1 has shown that stimulus intensity-dependent normalization persists under artificial stimulation[15]. However, optogenetic stimulation activates neurons regardless of visual response properties—sometimes referred to as 'hijacking' the circuit[54,55]. By contrast, nicotine acts on endogenous receptor machinery at the thalamocortical synapse, modulating the gain of incoming visual information. That our effects are well captured by a normalization model of (endogenous) attention suggests that this pharmacological perturbation engages the circuit's natural computational architecture, rather than overriding it. The focal nature of our gain perturbations means that they were inherently localized in both retinotopic and orientation space, allowing us to begin constraining the full two-dimensional gain field posited by normalization models. In-progress experiments in our lab using tangential penetrations aim to constrain a larger region of the model surface (gray in Fig. 5C), and to increase the number of 'no net effect' neurons that yield strong model constraints.

Prediction accuracy did not improve for infragranular units when we implemented a 'cascade' model that reflected the canonical V1 feedforward circuit (4C→supra→infragranular), yet evidence from columnar recordings with attentional modulation clearly supports different constraints for supragranular and infragranular layers[52,53]. While direct pathways from layer 4C to layers 5 and 6 exist[42–46], we suspect the outcome of our cascade analysis was due to weak model constraints. In particular, on too few days did we have adequate numbers of *both* supragranular and infragranular units.

Normalization models of attention assert that the suppressive pool inherits gain from the stimulus drive. The standard model modestly outperformed a variant in which the suppressive pool is blind to the gain field (i.e., normalization operates on the unmodulated stimulus drive; 82.6% vs. 76.9% prediction accuracy). However, the predicted suppression magnitude for the variant was weak (minimum predicted response area, N:S RA = 0.80); our observed suppression was stronger than this, supporting the standard model.

So what can the model tell us about biology? As noted above, on a day when we had the fluid port misplaced (in layer 4B), this could be diagnosed from fitted parameters, which converged on gain field tuning corresponding to the tuning of the nearest layer 4C neurons. Beyond this, the normalization model has two scale parameters governing the gain field: across retinotopic (AxWidth) and orientation (AθWidth) space. In our application, the model was relatively insensitive to AxWidth (Supplementary Fig. S4), likely because our columnar recordings sampled a narrow range of retinotopic positions. AθWidth, by contrast, was well constrained and the primary source of between-session variability. Fitted values clustered bimodally—four

sessions at 4° and four at ~12°—with no relationship to nicotine concentration (see below). This may reflect local orientation map architecture: In species with a columnar orientation map in V1, neurons in regions known as ‘pinwheels’ have broader orientation tuning than do neurons in iso-orientation domains[56–60]. Within an iso-orientation domain, a narrow AθWidth likely suffices, whereas near a pinwheel center, where orientation preferences are diverse, a broader field is required. Future experiments incorporating optical imaging of orientation maps could address this directly.

Not only did AθWidth not correlate with the concentration of the nicotine solution; none of the fitted parameters describing the gain field did. This is consistent with the gain field’s spatial extent being determined by features such as the local orientation map and the number of nAChRs within the diffusion radius. We expect that the action of ACh itself would be similarly determined by circuit features.

Finally, we modeled the saline condition as a distributed attention, rather than unattended, condition. The fitted gain field for saline trials (AxWidth = 7.5, in units of ~2 × eccentricity; AθWidth = 90°) suggests distributed attention across the central ~4° of the visual field, broadly tuned for orientation. The model thus implies that in our task animals are “attending” narrowly in space—perhaps to maintain fixation while stimuli are presented parafoveally—and not to stimulus orientation.

Our model fits 37 parameters to 121 observations; overfitting is a concern. However, effective flexibility is lower than this suggests: 1) the model is fit to ternary class labels, not continuous magnitudes (shuffled labels yield only 62% accuracy); 2) two per-day parameters are constrained by independent measurements; 3) the five global parameters must explain structure across all 121 units simultaneously; and 4) day-specific parameters cannot compensate for poor fits to other days. Furthermore, gain magnitudes—not used in fitting—are correlated with predictions (Fig. 6), providing independent support that the model captures real structure.

Our behavioral data (Fig. 7) show that the gain changes induced by nicotine yield biased perceptual performance that is consistent with the predictions of normalization models of attention. That modulation of activity in a tiny tissue volume can measurably change behavior speaks to the power of controlling the ‘gate’ to cortex. The strong expression of modulatory receptors—across species, at this point in the circuit[1–3,5,8,9,24,33,34,36]—suggests that evolution also ‘discovered’ this means by which the brain can modify its own activity.

Whether attention's demonstrated joint selectivity for location and feature[61–64] requires separate top-down signals or can emerge from a single gain field has been difficult to determine. Our data suggest a parsimonious answer for one level of the cortical hierarchy: Because V1 layer 4C neurons are organized in a joint map of retinotopic position and orientation preference, focal gain modulation here is inherently jointly tuned—the anatomy does the work. Any system that can deliver gain to a specific layer 4C location achieves joint modulation without requiring separate mechanisms for each dimension. The normalization model handles this intrinsically, and our data confirm its predictions for the joint case.

ACh itself is hypothesized to support attention; could cholinergic gain control of thalamocortical transmission be ‘the’ mechanism of attention? Strictly speaking, almost certainly not: Although the capacity of the cholinergic system to specifically address such a precise point (~1mm) in cortex has not been determined, it would require some exotic (although biologically feasible[70]) circuitry to do so. In a study that delivered cholinergic agents by iontophoresis without targeting layer 4C, Herrero et al[71] showed that muscarinic antagonists reduced attentional modulation of V1 responses, which suggests that muscarinic receptors are expressed in V1 in a way that allows them to engage endogenous machinery that supports attention. Without directly targeting layer 4C (where nAChRs are expressed), that study did not address any nicotinic component of endogenous attentional modulation. Importantly: In our study, neurons outside layer 4C did not ‘know’ that we used nicotine to inject gain; they just saw the gain field change. From that standpoint, we show that if you want to achieve tuned contrast enhancement of a visual stimulus (and this is certainly one of the things visual attention does[40,63,72]), gain control at the thalamocortical synapse could do the job.

Methods

Animals

One adult male (D, age 10) and one adult female (E, age 12) *Macaca mulatta* were used in this study. Animals were socially housed in an AAALAC-certified facility at Duke University on a 12-hour light/dark cycle in humidity and temperature controlled environments. All procedures were approved by Duke University's Institutional Animal Care and Use Committee, in accordance with NIH guidelines. Both animals were maintained on *ad libitum* food and water in their home cages throughout the study.

Behavior

Behavioral control and monitoring: During task performance and recording, animals were seated in a dimly lit (< 1 cd/m^2) Faraday room and monitored continuously via infrared camera. Eye position and pupil size were monitored non-invasively using a high-speed infrared eye tracking system (EyeLink). Visual stimuli were delivered by a ProPixx projector (VPixx) onto the central 73.5 x 40.5 cm of a 122 x 91 cm (W x H) polarization-preserving rear projection screen (Stewart Filmscreen) positioned 98.5 cm from the eyes. Animals were head fixed using the Thomas Recording titanium 3-post mini plate + 'Halo' system (Thomas Primate Positioning System).

Passive Fixation Task: Animals were trained to maintain fixation within 1.0 degree of visual angle (dva) of a fixation point at the center of the screen while Gabor stimuli of varying position, orientation, and contrast (fixed diameter = 2 dva and spatial frequency = 1.5 cycles/degree, cpd) were presented for 150-ms on/off periods on a 20 cd/m^2 mean gray background (Fig. 1A). ~0.2 mL dilute juice reward was delivered for correctly maintaining fixation throughout the full fixation period. In one animal (D) the Gabor stimuli were static; in the other (E) they were drifting.

Perceptual Equivalence Task: One animal (E) was trained to fixate (as described for passive fixation, above). After a period of 750-1750 ms, two static Gabor stimuli appeared simultaneously, one in each hemifield. Stimuli were identical in size, spatial frequency, temporal frequency, and orientation, but differed in contrast. Trials were randomly interleaved for two series of contrast comparisons against a) 20% and b) 40% contrast 'target' Gabors. Stimuli for comparison were generated representing three half-steps, and presented in randomized order using the method of constant stimuli (see Fig. 7A). The animal was trained to saccade to the higher contrast stimulus. A juice reward was delivered for correct choices; choices between identical stimuli were randomly rewarded. To prevent reward feedback interfering with nicotine effects on perception, during the nicotine delivery window a probabilistic reward was enacted such that stimuli that differed by 3% contrast or less were rewarded with probability 0.75, regardless of choice.

Behavioral Analysis

Performance was analyzed by combining trials across the two reference/pedestal contrasts (20% and 40%) after normalizing comparison contrasts to the reference (yielding a common set of contrast ratios: 0, 0.5, 0.75, 1.0, 1.25, 1.5, and 2.0). For each session, drug condition, and hemifield, we computed the proportion of trials on which the animal chose the comparison stimulus at each contrast ratio. Logistic functions of the form

$$p = \frac{a}{1+e^{-b(x-c)}}$$

were fit to these curves using nonlinear least-squares regression (MATLAB Curve Fitting Toolbox), and the point of subjective equivalence (PSE) extracted as the contrast ratio yielding p = 0.5. We found no difference in behavioral performance between baseline (no delivery) and saline conditions, and so these trials were combined in comparison with nicotine.

To test the normalization model's directional prediction, we computed a composite score for each session capturing the net change in rightward choice bias under nicotine. For each hemifield, we calculated the mean proportion chosen at contrast ratios ≥ 0.75 (spanning the dynamic range of the psychometric function) under nicotine and under saline. The composite was defined as (right_nicotine − right_saline) − (left_nicotine − left_saline), representing the net shift in rightward bias. This composite was then direction-corrected by the model prediction: multiplied by +1 for co-tuned sessions (where nicotine is predicted to increase rightward apparent contrast) and by −1 for non-co-tuned sessions (where nicotine is predicted to decrease it). A positive direction-corrected composite indicates a shift in the predicted direction. Statistical significance was assessed using a two-tailed binomial sign test (n = 6 sessions) and a one-sample t-test against zero.

Electrophysiology

The combined electrophysiology and nicotine delivery experiments were conducted using 32-channel S-Probes (Plexon; PLX-SP-32-15SE(100)-(260-100)(640-30)-640-FC16/17-(1)CON/32m-V). Electrode spacing on these arrays was at 100 µm pitch, and a fluid capillary allowing for drug delivery exited the probe between electrodes 16 and 17 (Fig. 1C). Data were recorded using Synapse software from Tucker Davis Technologies (TDT) at a sampling rate of ~24,414 kHz, amplified using the TDT PZ5 and RZ2 bioamp processors, band pass filtered (0.3 to 10 kHz), and stored for offline analysis.

S-Probes were positioned using a motorized drive (Thomas Recording), with a sharpened stainless steel guide tube to assist in passing dura. Using a single unit electrode (FHC), dura thickness was measured before the first recordings were made, and the approximate daily thickness estimated based on changes in height from the chamber top. Using these estimates, guide tube tips were positioned just before cortex (i.e., still within dura) and the stainless steel-tipped S-probe used to exit dura and enter cortex. Electrodes were advanced at a drive speed of 2 µm/second until the uppermost channel was estimated to be just above, or within, layer 1.

Array positioning with respect to the granular layer was determined by current source density (CSD) analysis calculated from a 2-3-minute recording of local field potential responses to 100 ms flashes of 100% contrast, full-field gratings (1.5 cpd), presentation of which was initiated any time the eyes were on the screen. Electrode position was adjusted as needed to place the fluid capillary exit ('fluid port') in the early granular layer CSD sink (Fig. 1C).

Receptive field x-y position was mapped using flashed Gabor stimuli (22.5° steps, 2 dva, 1.5 cpd, 96% contrast, randomly interleaved). Orientation tuning preference was measured using Gabor stimuli (22.5° steps, randomly interleaved including blanks). In one animal orientation tuning was obtained (static Gabors; Monkey D); in the other direction tuning (drifting Gabors; Monkey E). Based on the observed receptive field positions and tuning preferences across the recording array, a 'best-fit' stimulus (x-y position and orientation/direction tuning) was chosen for use in measuring contrast gain. Contrast gain was measured in 9 logarithmic steps from 1% to 96%, plus 0% contrast 'blanks' (all randomly interleaved).

Pharmacology

Nicotine (Glentham Life Sciences; cat#65-31-6) was weighed and mixed in solution with sterile saline, pH adjusted to 4.5-7.0, and filtered at 0.22 µm prior to loading into electrodes for use. Pre-mixed solution was kept at 4°C for up to 7 days, after which a fresh solution was prepared. Nicotine concentration varied across days between 200-500 mM. At the start of each recording day the fluid capillary was filled with saline and connected to the pneumatic pump via microtubing filled with nicotine solution.

The estimated maximum total volume delivered for a given day was ~1-2 µL. Solutions (saline and nicotine) were delivered by pressure ejection (WPI pneumatic PicoPump PV830 or a Medical Systems Corp PLI_100, depending on the rig used for recording).

Saline or nicotine delivery occurred between the onset of fixation and presentation of the first stimulus. An electrode-specific pressure range was determined *ex vivo* based on calibration under a microscope (volume estimation from measured droplet size). Backing pressures used in each recording session were selected based on response stationarity (qualitatively assessed) for electrodes flanking the fluid port. Final pressure used for saline and nicotine delivery ranged from 2.5-20 PSI. After pressure was determined, the estimated number of delivery pulses to clear the fluid capillary of saline was calculated based on fluid capillary internal diameter and length measurements (Plexon). The saline condition trials were constrained by this maximum value. At the conclusion of the saline delivery condition, a 1-10-minute priming period existed prior to the first nicotine condition to ensure the fluid capillary was primed with nicotine solution and all saline had been ejected. Between 2 and 3 nicotine conditions were collected with differing backing pressure. Nicotine pressure conditions were always collected in order from lowest backing pressure to highest. The highest nicotine 'dose' was the one with backing pressure matched to the saline condition that yielded stable results. Either two (~30-50% and 100% of the maximum dose) or three (33%, 66%, and 100% doses) were tested.

Data Processing and Analysis:

Spike recording, sorting, and windowing: Waveforms were sorted offline in MATLAB (MathWorks) using sorting code developed by Dr. K. Nielsen at Johns Hopkins University (available on the nielsenlab GitHub

repository)[73]. Thresholds were individually set per channel and sorts were based on multiple waveform characteristics (spike amplitude maximum, minimum, and spike width). Response window start times were calculated for each trial for each unit individually by calculating a per-trial baseline (average and standard deviation, sd, of spike rate in the first 20 ms after stimulus onset) and then finding the first 10 ms window during which the average spike rate was more than 4 sd over baseline for the response window start. Response window length was 150 ms.

Inclusion criteria for analysis: Permissive inclusion criteria were used: units needed to have (1) a clear receptive field position, (2) a spike rate difference > 1 spike/sec between the peak and trough of the orientation tuning fit, (3) an average spiking response to the 96% contrast stimulus at least 1 sd higher than the average response to the 0% contrast blank, (4) an average response to the 96% contrast stimulus under the no-fluid delivery baseline of > 1 spike/sec, and (5) (for supragranular and infragranular only) a response that was not significantly suppressed by saline delivery, determined by a bootstrap analysis on the normalized response area (see Non-parametric analysis). Additional visual inspection of rasters per unit ensured responses to stimuli were not lost during fluid delivery.

Receptive field size and position were fit with a 2D gaussian function, and double von Mises fits were applied to orientation/direction tuning, yielding the peak (preferred) orientation used for comparison with stimulus orientation.

Parametric analysis of contrast responses: A hyperbolic ratio (Naka-Rushton) function (Eq. 2) was fit for each condition (baseline, saline, drug) to the averaged (across 39-247 repeats) responses, R, for each stimulus contrast, C:

$$R = R_{max}\left(\frac{C^n}{C^n + C_{50}^n}\right) + sFR \qquad \text{Eq. 2}$$

This fit yields four parameters: Rmax (maximum response), c50 (contrast at the half-maximum response), n (function slope), and sFR (offset attributable to 'spontaneous' firing). A bootstrap analysis was performed by sampling randomly from responses to each contrast and fitting. To classify gain types, we used bootstrap fits computed from 1000 iterations of resampling with replacement from single-trial firing rates at each contrast level. Neurons with c50 estimates exceeding 95% contrast or Rmax below 1 spike/sec in more than half of bootstrap iterations were excluded (4/121). Wilcoxon rank-sum tests compared the 1000 saline and nicotine bootstrap values of Rmax and c50 for each neuron, with p-values corrected across all units using the Benjamini-Hochberg procedure (FDR alpha = 0.05). Direction was assigned from the ratio of bootstrap medians. Model-predicted Rmax and c50 were obtained by fitting Naka-Rushton functions to the predicted contrast response functions (CRFs). Consistency was assessed by testing whether predicted ratios fell within conservative confidence intervals derived from the bootstrapped distribution.

Non-parametric analysis of contrast responses: We obtained an approximate 'area under the curve' measure, which we call the normalized response area (RA). To obtain this measure, we calculated the average firing rate response to each stimulus contrast, subtracted from this the average firing rate to a blank screen, and then normalized to the firing rate response for the highest stimulus contrast (96%) under the control condition relevant for the comparison (no drug baseline or pressure-matched saline). We then summed these normalized, 'blank-subtracted' spike rates across all contrasts, and expressed them as a ratio of the experimental to control condition (e.g., nicotine divided by saline; N:S RA)[24]. Both parametric (t-test) and non-parametric (Wilcoxon signed-rank) statistics were calculated and exact p-values reported.

Normalization Model of Attention

We used both publicly-available scripts (https://snl.salk.edu/~reynolds/Normalization_Model_of_Attention/) and our own custom MATLAB code for this analysis.

Using port tuning as priors on Ax, Aθ, and AθWidth: The nicotine attention field center was constrained by independent measurements at the fluid port. The spatial center (Ax) was initialized from the receptive field location mapped for channels 16 and 17, which flanked the capillary exit port. The orientation center (Aθ) was similarly initialized from orientation tuning measured at these same electrodes. As a prior on the orientation

width (AθWidth) of the attention field, we used the peak location from double von Mises fits to spiking responses as a function of stimulus orientation for four electrodes neighboring the port (channels 15–18). Each von Mises fit was assigned a confidence weight (1.0 for well-isolated units with clear tuning; 0.5 for noisy, weakly tuned, or multi-unit estimates; excluded if no responsive units were present) and a distance weight that decayed with electrode distance from the port (channels 16–17 received full weight; more distant channels were downweighted as 1/distance). The circular variance of the weighted orientation preferences provided an empirical estimate of the orientation diversity across the neural population at the nicotine delivery site, which served as a plausibility check on the fitted nicotine gain field width (nicotine AθWidth).

Fitting the model: We fit the normalization model to the observed nicotine/saline response ratios using a hierarchical optimization procedure. Parameters were divided into two classes: per-session parameters describing the nicotine gain field for each recording day (peak gain, Apeak; baseline gain, Abase; orientation center, Aθ; orientation tuning width, AθWidth; and spatial center, Ax), and global parameters shared across all sessions (saline spatial and orientation gain field width: salAxWidth and salAθWidth, respectively; nicotine spatial gain field width, nicAxWidth; excitatory and inhibitory kernels for mode unit orientation tuning: EθWidth and IθWidth, respectively). The model was thus fit with 5 free parameters per session (Apeak, Abase, Aθ, AθWidth, Ax) and 5 shared parameters optimized across sessions (nicAxWidth, salAxWidth, salAθWidth, EθWidth, IθWidth), totaling 37 free parameters for 121 observations. Because the loss function operates on sign classifications rather than continuous values, the effective information per observation is less than one bit, making direct comparison of parameter count to observation count conservative—many parameter configurations produce identical sign predictions; three of the continuous parameters are further constrained by the port tuning measurements.

For each recording day, each neuron's position in model space was determined by projecting its receptive field location onto the stimulus axis (a vector from central fixation through the center of the visual stimulus position) and computing its preferred orientation relative to the stimulus orientation. The model predicted a nicotine/saline response ratio (N:S RA) for each neuron by computing the full normalization equation under both nicotine and saline gain field configurations at peak contrast (96%; a measure of response gain) and across all tested contrasts (RA). The loss function counted the number of sign mismatches between predicted and observed ratios, classifying each neuron as having an increased (N:S RA > 1.01), decreased (ratio < 0.99), or unchanged response area. Optimization proceeded in three stages: first, independent per-session fits were performed with global parameters fixed at initial estimates; second, global and per-session parameters were alternately optimized, iterating until convergence; and third, a final per-session refit was performed with the converged global parameters held fixed.

There is an inherent degeneracy in the normalization model: both the excitatory drive and the suppressive pool are scaled by the attention field. The predicted response ratio thus depends on the contrast between peak (Apeak) and baseline (Abase) gain, not on their absolute values. To address this degeneracy, Abase and Apeak were fit independently along two optimization paths that released these parameters in opposite order, and the lower-loss solution was retained. We report fitted results as gain field contrast (Abase/Apeak; Table 1). This parameterization does not assume a specific correspondence between Apeak and the magnitude of nicotinic receptor activation; rather, it provides a normalized coordinate system in which the spatial and orientation structure of nicotine's modulatory field can be compared across sessions.

Direct versus cascade models for infragranular units: To test whether infragranular responses could be better explained by a model that respects the canonical feedforward circuit from supragranular to infragranular layers, we compared two approaches for predicting infragranular effects. In a ‘direct’ model, infragranular units are treated identically to supragranular units: each unit's predicted response is determined by its position relative to the same nicotine gain field, with no distinction between layers. In the ‘cascade’ model, infragranular neurons receive their excitatory input not from the stimulus modulated by the gain field, but from the output of the supragranular population after it has been processed through the first normalization stage. In this cascade model, the nicotine effect on infragranular units is inherited indirectly: the gain field reshapes the supragranular population response surface, and that reshaped output serves as the drive to a second normalization stage. The two stages are blended by a mixing parameter alpha, where alpha = 1 recovers the direct model and alpha = 0 represents the pure cascade. The second-stage excitatory and inhibitory pooling

kernels (ExWidth, IxWidth, EθWidth, IθWidth) were set to match the first-stage values. For both models, global and per-day parameters were held at values fitted to the supragranular data; infragranular predictions were therefore entirely out of sample. We evaluated each model by computing the sign accuracy of its predictions for infragranular units across a range of alpha values (0 to 1 in steps of 0.1). We additionally compared a refit-widths model, in which infragranular units receive the nicotine gain field directly, but with the spatial and orientation widths of the field scaled by a multiplicative factor (swept from 0.5 to 3.0), representing the possibility that the effective gain field is broader or narrower in infragranular layers due to differences in local connectivity.

Evaluating model performance: To assess whether the normalization model captures genuine structure in the data rather than achieving accuracy by overfitting to the base rates of enhancement and suppression, we performed a permutation test. For each of 1000 permutations, the observed effect labels (increased, decreased, or unchanged RA, as described above for model fitting) were randomly shuffled across units independently within each recording day, preserving the per-day proportions of each class. The full model-fitting procedure was then applied to the shuffled labels: for each day, the five per-day parameters (Apeak, Abase, AθWidth, Ax, Aθ) were optimized by minimizing the sign-based loss function against the shuffled labels, with global parameters held fixed at their previously determined (optimized) values. Sign accuracy was computed for each permutation, yielding a null distribution of accuracy values achievable when the spatial and featural relationship between unit positions and effect labels is destroyed. The real data accuracy was then compared to this null distribution, with the p-value computed as the proportion of permutations achieving accuracy equal to or greater than the real data (with a +1 correction in numerator and denominator to avoid p = 0). This procedure controls for the possibility that the model's free parameters could accommodate arbitrary label assignments. To assess the contribution of orientation tuning to model performance, we compared the full joint model against a position-only variant. In the position-only model, the per-day orientation bandwidth of the nicotine gain field was set to 180° (uniform across all orientations), while all other parameters—including the gain field peak (Apeak), spatial center (Ax), orientation center (Aθ), and all global parameters—were held at their fitted values. Sign accuracy and Spearman correlations were computed for both models using the same classification thresholds and compared to the shuffled-label null distribution.

References

1. Disney, A.A. (2021). Neuromodulatory Control of Early Visual Processing in Macaque. Annu Rev Vis Sci *7*, 181–199.

2. Rakic, P., Goldman-Rakic, P.S., and Gallager, D. (1988). Quantitative autoradiography of major neurotransmitter receptors in the monkey striate and extrastriate cortex. J. Neurosci. *8*, 3670–3690.

3. Watakabe, A., Komatsu, Y., Sadakane, O., Shimegi, S., Takahata, T., Higo, N., Tochitani, S., Hashikawa, T., Naito, T., Osaki, H., et al. (2009). Enriched expression of serotonin 1B and 2A receptor genes in macaque visual cortex and their bidirectional modulatory effects on neuronal responses. Cereb. Cortex *19*, 1915–1928.

4. Han, Z.-Y., Zoli, M., Cardona, A., Bourgeois, J.-P., Changeux, J.-P., and Le Novère, N. (2003). Localization of [3H]nicotine, [3H]cytisine, [3H]epibatidine, and [125I]alpha-bungarotoxin binding sites in the brain of Macaca mulatta. J. Comp. Neurol. *461*, 49–60.

5. Prusky, G.T., Shaw, C., and Cynader, M.S. (1987). Nicotine receptors are located on lateral geniculate nucleus terminals in cat visual cortex. Brain Res. *412*, 131–138.

6. Cremer, C.M., Lübke, J.H.R., Palomero-Gallagher, N., and Zilles, K. (2011). Laminar distribution of neurotransmitter receptors in different reeler mouse brain regions. Brain Struct. Funct. *216*, 201–218.

7. Jacob, S.N., and Nienborg, H. (2018). Monoaminergic Neuromodulation of Sensory Processing. Front. Neural Circuits *12*, 51.

8. Zilles, K., and Palomero-Gallagher, N. (2017). Multiple transmitter receptors in regions and layers of the human cerebral cortex. Front. Neuroanat. *11*, 78.

9. Rapan, L., Niu, M., Zhao, L., Funck, T., Amunts, K., Zilles, K., and Palomero-Gallagher, N. (2022). Receptor architecture of macaque and human early visual areas: not equal, but comparable. Brain Struct. Funct. *227*, 1247–1263.

10. Gu, Q. (2002). Neuromodulatory transmitter systems in the cortex and their role in cortical plasticity. Neuroscience *111*, 815–835.

11. Yang, Y., Paspalas, C.D., Jin, L.E., Picciotto, M.R., Arnsten, A.F.T., and Wang, M. (2013). Nicotinic α7 receptors enhance NMDA cognitive circuits in dorsolateral prefrontal cortex. Proc. Natl. Acad. Sci. U.S.A. *110*, 12078–12083.

12. Goldman-Rakic, P.S., Lidow, M.S., and Gallager, D.W. (1990). Overlap of dopaminergic, adrenergic, and serotoninergic receptors and complementarity of their subtypes in primate prefrontal cortex. J. Neurosci. *10*, 2125–2138.

13. Wang, M., Ramos, B.P., Paspalas, C.D., Shu, Y., Simen, A., Duque, A., Vijayraghavan, S., Brennan, A., Dudley, A., Nou, E., et al. (2007). α2A-Adrenoceptors Strengthen Working Memory Networks by Inhibiting cAMP-HCN Channel Signaling in Prefrontal Cortex. Cell *129*, 397–410.

14. Paspalas, C.D., and Goldman-Rakic, P.S. (2005). Presynaptic D 1 Dopamine Receptors in Primate Prefrontal Cortex: Target-Specific Expression in the Glutamatergic Synapse. J. Neurosci. *25*, 1260–1267.

15. Nassi, J.J., Avery, M.C., Cetin, A.H., Roe, A.W., and Reynolds, J.H. (2015). Optogenetic activation of normalization in alert macaque visual cortex. Neuron *86*, 1504–1517.

16. Sanzeni, A., Palmigiano, A., Nguyen, T.H., Luo, J., Nassi, J.J., Reynolds, J.H., Histed, M.H., Miller, K.D., and Brunel, N. (2023). Mechanisms underlying reshuffling of visual responses by optogenetic stimulation in mice and monkeys. Neuron *111*, 4102–4115.e9.

17. Fenoy, A.J., Severson, M.A., Volkov, I.O., Brugge, J.F., and Howard, M.A., 3rd (2006). Hearing suppression induced by electrical stimulation of human auditory cortex. Brain Res. *1118*, 75–83.

18. Mégevand, P., Groppe, D.M., Goldfinger, M.S., Hwang, S.T., Kingsley, P.B., Davidesco, I., and Mehta, A.D. (2014). Seeing scenes: topographic visual hallucinations evoked by direct electrical stimulation of the parahippocampal place area. J. Neurosci. *34*, 5399–5405.

19. Mihai, F., Tofan, L., Barborica, A., Oane, I., Zagrean, A.-M., Lentoiu, C., Ghita, C., and Mindruta, I. (2025).

Multi-modal connectivity of the brain underlying visual hallucinations evoked by high-frequency intracranial stimulations. Brain Stimul. *18*, 1141–1149.

20. Jazayeri, M., Lindbloom-Brown, Z., and Horwitz, G.D. (2012). Saccadic eye movements evoked by optogenetic activation of primate V1. Nat. Neurosci. *15*, 1368–1370.

21. Murphey, D.K., and Maunsell, J.H.R. (2007). Behavioral detection of electrical microstimulation in different cortical visual areas. Curr. Biol. *17*, 862–867.

22. De, A., El-Shamayleh, Y., and Horwitz, G.D. (2020). Fast and reversible neural inactivation in macaque cortex by optogenetic stimulation of GABAergic neurons. Elife *9*, e52658.

23. Tehovnik, E.J., and Slocum, W.M. (2013). Electrical induction of vision. Neurosci. Biobehav. Rev. *37*, 803–818.

24. Disney, A.A., Aoki, C., and Hawken, M.J. (2007). Gain modulation by nicotine in macaque v1. Neuron *56*, 701–713.

25. Sato, H., Hata, Y., Hagihara, K., and Tsumoto, T. (1987). Effects of cholinergic depletion on neuron activities in the cat visual cortex. J. Neurophysiol. *58*, 781–794.

26. Herrero, J.L., Roberts, M.J., Delicato, L.S., Gieselmann, M.A., Dayan, P., and Thiele, A. Supplementary Materials: Acetylcholine contributes to attentional modulation in V1 by muscarinic receptors. https://doi.org/10.1038/nature1.

27. Servan-Schreiber, D., Printz, H., and Cohen, J.D. (1990). A network model of catecholamine effects: gain, signal-to-noise ratio, and behavior. Science *249*, 892–895.

28. Aston-Jones, G., and Cohen, J.D. (2005). An integrative theory of locus coeruleus-norepinephrine function: adaptive gain and optimal performance. Annu. Rev. Neurosci. *28*, 403–450.

29. Yu, A.J., and Dayan, P. (2005). Uncertainty, neuromodulation, and attention. Neuron *46*, 681–692.

30. Deco, G., and Thiele, A. (2011). Cholinergic control of cortical network interactions enables feedback-mediated attentional modulation: Cholinergic control of cortical network interactions. Eur. J. Neurosci. *34*, 146–157.

31. Reynolds, J.H., and Heeger, D.J. (2009). The normalization model of attention. Neuron *61*, 168–185.

32. Ni, A.M., and Maunsell, J.H.R. (2017). Spatially tuned normalization explains attention modulation variance within neurons. J. Neurophysiol. *118*, 1903–1913.

33. Gil, Z., Connors, B.W., and Amitai, Y. (1997). Differential regulation of neocortical synapses by neuromodulators and activity. Neuron *19*, 679–686.

34. Hsieh, C.Y., Cruikshank, S.J., and Metherate, R. (2000). Differential modulation of auditory thalamocortical and intracortical synaptic transmission by cholinergic agonist. Brain Res. *880*, 51–64.

35. Kruglikov, I., and Rudy, B. (2008). Perisomatic GABA release and thalamocortical integration onto neocortical excitatory cells are regulated by neuromodulators. Neuron *58*, 911–924.

36. Kimura, F., Fukuda, M., and Tsumoto, T. (1999). Acetylcholine suppresses the spread of excitation in the visual cortex revealed by optical recording: possible differential effect depending on the source of input. Eur. J. Neurosci. *11*, 3597–3609.

37. Garwood, I.C., Major, A.J., Antonini, M.-J., Correa, J., Lee, Y., Sahasrabudhe, A., Mahnke, M.K., Miller, E.K., Brown, E.N., and Anikeeva, P. (2023). Multifunctional fibers enable modulation of cortical and deep brain activity during cognitive behavior in macaques. Sci. Adv. *9*, eadh0974.

38. Dagdeviren, C., Ramadi, K.B., Joe, P., Spencer, K., Schwerdt, H.N., Shimazu, H., Delcasso, S., Amemori, K.-I., Nunez-Lopez, C., Graybiel, A.M., et al. (2018). Miniaturized neural system for chronic, local intracerebral drug delivery. Sci. Transl. Med. *10*, eaan2742.

39. Reynolds, J.H., Pasternak, T., and Desimone, R. (2000). Attention increases sensitivity of V4 neurons. Neuron *26*, 703–714.

40. Williford, T., and Maunsell, J.H.R. (2006). Effects of spatial attention on contrast response functions in macaque area V4. J. Neurophysiol. *96*, 40–54.

41. Lee, J., and Maunsell, J.H.R. (2010). The effect of attention on neuronal responses to high and low contrast stimuli. J. Neurophysiol. *104*, 960–971.

42. Yabuta, N.H., and Callaway, E.M. (1998). Functional streams and local connections of layer 4C neurons in primary visual cortex of the macaque monkey. J. Neurosci. *18*, 9489–9499.

43. Callaway, E.M., and Wiser, A.K. (1996). Contributions of individual layer 2-5 spiny neurons to local circuits in macaque primary visual cortex. Vis. Neurosci. *13*, 907–922.

44. Lund, J.S. (1987). Local circuit neurons of macaque monkey striate cortex: I. Neurons of laminae 4C and 5A. J. Comp. Neurol. *257*, 60–92.

45. Fitzpatrick, D., Lund, J.S., and Blasdel, G.G. (1985). Intrinsic connections of macaque striate cortex: afferent and efferent connections of lamina 4C. J. Neurosci. *5*, 3329–3349.

46. Briggs, F., and Callaway, E.M. (2005). Laminar patterns of local excitatory input to layer 5 neurons in macaque primary visual cortex. Cereb. Cortex *15*, 479–488.

47. Vogels, R., and Orban, G.A. (1991). Quantitative study of striate single unit responses in monkeys performing an orientation discrimination task. Exp. Brain Res. *84*, 1–11.

48. De Valois, R.L., William Yund, E., and Hepler, N. (1982). The orientation and direction selectivity of cells in macaque visual cortex. Vision Res. *22*, 531–544.

49. Ringach, D.L., Shapley, R.M., and Hawken, M.J. (2002). Orientation selectivity in macaque V1: Diversity and laminar dependence. J. Neurosci. *22*, 5639–5651.

50. Heeger, D.J. (1992). Normalization of cell responses in cat striate cortex. Vis. Neurosci. *9*, 181–197.

51. Carandini, M., and Heeger, D.J. (2011). Normalization as a canonical neural computation. Nat. Rev. Neurosci. *13*, 51–62.

52. Nandy, A.S., Nassi, J.J., and Reynolds, J.H. (2017). Laminar organization of attentional modulation in macaque visual area V4. Neuron *93*, 235–246.

53. Ferro, D., van Kempen, J., Boyd, M., Panzeri, S., and Thiele, A. (2021). Directed information exchange between cortical layers in macaque V1 and V4 and its modulation by selective attention. Proc. Natl. Acad. Sci. U. S. A. *118*, e2022097118.

54. Cheney, P.D., Griffin, D.M., and Van Acker, G.M., 3rd (2013). Neural hijacking: action of high-frequency electrical stimulation on cortical circuits: Action of high-frequency electrical stimulation on cortical circuits. Neuroscientist *19*, 434–441.

55. Griffin, D.M., Hudson, H.M., Belhaj-Saïf, A., and Cheney, P.D. (2011). Hijacking cortical motor output with repetitive microstimulation. J. Neurosci. *31*, 13088–13096.

56. Ikezoe, K., Mori, Y., Kitamura, K., Tamura, H., and Fujita, I. (2013). Relationship between the local structure of orientation map and the strength of orientation tuning of neurons in monkey V1: a 2-photon calcium imaging study. J. Neurosci. *33*, 16818–16827.

57. Nauhaus, I., Benucci, A., Carandini, M., and Ringach, D.L. (2008). Neuronal selectivity and local map structure in visual cortex. Neuron *57*, 673–679.

58. Obermayer, K., and Blasdel, G.G. (1993). Geometry of orientation and ocular dominance columns in monkey striate cortex. J. Neurosci. *13*, 4114–4129.

59. Blasdel, G.G. (1992). Orientation selectivity, preference, and continuity in monkey striate cortex. J. Neurosci. *12*, 3139–3161.

60. Bonhoeffer, T., and Grinvald, A. (1991). Iso-orientation domains in cat visual cortex are arranged in pinwheel-like patterns. Nature *353*, 429–431.

61. Treue, S., and Martínez Trujillo, J.C. (1999). Feature-based attention influences motion processing gain

in macaque visual cortex. Nature *399*, 575–579.

62. McAdams, C.J., and Maunsell, J.H. (1999). Effects of attention on orientation-tuning functions of single neurons in macaque cortical area V4. J. Neurosci. *19*, 431–441.

63. Reynolds, J.H., and Chelazzi, L. (2004). Attentional modulation of visual processing. Annu. Rev. Neurosci. *27*, 611–647.

64. Maunsell, J.H.R., and Treue, S. (2006). Feature-based attention in visual cortex. Trends Neurosci. *29*, 317–322.

65. Disney, A.A., and Higley, M.J. (2020). Diverse Spatiotemporal Scales of Cholinergic Signaling in the Neocortex. J. Neurosci. *40*, 720–725.

66. Gu, Z., and Yakel, J.L. (2011). Timing-dependent septal cholinergic induction of dynamic hippocampal synaptic plasticity. Neuron *71*, 155–165.

67. Fiebelkorn, I.C., and Kastner, S. (2021). Spike timing in the attention network predicts behavioral outcome prior to target selection. Neuron *109*, 177–188.e4.

68. Martin, A.B., Yang, X., Saalmann, Y.B., Wang, L., Shestyuk, A., Lin, J.J., Parvizi, J., Knight, R.T., and Kastner, S. (2019). Temporal dynamics and response modulation across the human visual system in a spatial attention task: An ECoG study. J. Neurosci. *39*, 333–352.

69. Abdalaziz, M., Redding, Z.V., and Fiebelkorn, I.C. (2023). Rhythmic temporal coordination of neural activity prevents representational conflict during working memory. Curr. Biol. *33*, 1855–1863.e3.

70. Coppola, J.J., Ward, N.J., Jadi, M.P., and Disney, A.A. (2016). Modulatory compartments in cortex and local regulation of cholinergic tone. J. Physiol. Paris *110*, 3–9.

71. Herrero, J.L., Roberts, M.J., Delicato, L.S., Gieselmann, M.A., Dayan, P., and Thiele, A. (2008). Acetylcholine contributes through muscarinic receptors to attentional modulation in V1. Nature *454*, 1110–1114.

72. Ling, S., and Carrasco, M. (2006). Sustained and transient covert attention enhance the signal via different contrast response functions. Vision Res. *46*, 1210–1220.

73. Khamiss, D.C., Lempel, A.A., Nanfito, B.R., and Nielsen, K.J. (2025). Early development of direction selectivity in higher visual cortex. Neuroscience.